Atomic photoionization processes under magnification

F. Lépine and Ch. Bordas
Laboratoire de Spectrométrie Ionique et Moléculaire, UMR CNRS 5579, Bâtiment A. Kastler, 43 Boulevard du 11 Novembre 1918, 69622 Villeurbanne Cedex, France

C. Nicole and M. J. J. Vrakking
FOM Instituut voor Atoom en Molecuul Fysica (AMOLF), Kruislaan 407, 1098 SJ, Amsterdam, The Netherlands
(Received 7 January 2004; published 28 September 2004)

Recently, classical simulations of threshold photoionization in the presence of an electric field have shown that a clear distinction between direct and indirect trajectories followed by the outgoing electron can be observed in the patterns of electron impacts on a two-dimensional detector. Subsequently, slow photoelectron imaging experiments have been reported where this distinction could be observed in atomic xenon. Furthermore, using a magnifying electrostatic lens to improve the velocity-map imaging technique, oscillatory patterns were observed modulating the classical envelope that was measured in the experiments of Nicole et al. [Phys. Rev. Lett. **88**, 133001 (2002)]. This extension of slow photoelectron imaging, called photoionization microscopy, relies on the existence of interferences between various trajectories by which the electron moves from the atom to the plane of observation. In this article we present the main experimental results obtained both in slow photoelectron imaging and in photoionization microscopy. The formation of the interference pattern is discussed in the framework of a semiclassical model that is described in detail elsewhere. The qualitative information that can be drawn from the experiments is discussed, and the potential applications of photoionization microscopy are considered. Particular attention is paid to the role of continuum Stark resonances that appear between the saddle point in the Coulomb+dc field potential and the field-free ionization limit.

DOI: 10.1103/PhysRevA.70.033417 PACS number(s): 32.60.+i, 32.80.Fb, 07.81.+a, 32.80.Rm

I. INTRODUCTION

Since the pioneering work of Chandler and Houston [1], photoelectron and photofragment imaging techniques have undergone significant improvements and have opened the way to a wide range of studies not accessible previously, Among the technical improvements, the introduction of the velocity-map imaging method [2] by Eppink and Parker, which improved the resolution of the method by at least an order of magnitude, has been of the utmost importance. Other important recent improvements are the introduction of slice imaging [3], the introduction of many-particle three-dimensional (3D) imaging [4,5], and the introduction of multistage electron optics [6]. It is the last development that has made possible the experimental results presented in this work.

One of the many fields now accessible owing to the power of charged-particle imaging techniques is the ability to look with unprecedented precision at photodetachment [7] and photoionization processes. More specifically, photoelectron imaging allows a "magnifying glass" examination of photoionization in an external electric field. The motion of the electron ejected in photoionization in the presence of an electric field provides a textbook example of a situation where the quantum nature of the wave function can be observed in the macroscopic world. For that reason, part of the work presented below has been denoted photoionization microscopy since it allows one precisely to observe macroscopic images of the square modulus of the electronic wave function.

Despite being one of the oldest problems treated in the framework of quantum mechanics, the study of the Stark effect, especially in the continuum, still contains a number of unclear issues that deserve a renewed approach using state-of-the-art techniques. Among these, high-resolution velocity-map imaging is obviously one of the most powerful.

In this paper, we present a general description of the experimental results that we have obtained in photoionization imaging of a simple atom (namely, xenon) both in the case of intermediate-resolution experiments where a purely classical approach is sufficient to analyze the experimental results, and at high resolution where the quantum nature of the outgoing electron current appears explicitly in the image. In the latter case, our results are analyzed within the framework of the semiclassical model described in a series of papers by Kondratovich and Ostrovsky [8–11]. Some of the experimental results presented in this article have already been presented as Letters [12,13]. Their detailed interpretation has been discussed, respectively, in Refs. [14] and [15]. The present article is intended as a presentation of all the most prominent results as well as experimental results that were not discussed yet in the two Letters, and their discussion from a unified point of view.

In the subsequent presentation of our results, we have intentionally followed a pedagogic approach, starting with low-resolution slow photoelectron imaging, providing an overview of a series of phenomena that are almost fully interpretable in terms of classical mechanics, and leading ultimately to photoionization microscopy imaging, providing the square modulus of the amplitude of the outgoing wave packet. In that sense, we follow a zooming procedure in the photoionization process itself: from the naked eye to the magnifying glass, and from the magnifying glass to the microscope.

The organization of the paper is as follows. In Sec. II we recall the basic properties of classical electron trajectories under the combined effect of a static external electric field and a Coulomb field, with specific emphasis on the distinction between direct and indirect trajectories. We also summarize the semiclassical approach that is later used to interpret the formation of the interference patterns. The experimental arrangement used for studying photoionization of xenon in an external electric field is detailed in Sec. III. In Sec. IV we report the observations obtained when using a traditional velocity-map imaging setup and the peculiarities of slow electron imaging when the ballistic approximation that is normally used in two-dimensional imaging experiments is no longer valid. Section V is devoted to similar experiments in the case where the continuum Stark spectrum is resolved and where slow photoelectron imaging correlates the localization of the optically excited electron wave packet with the dynamics of direct or indirect photoionization. Photoionization microscopy is detailed in Sec. VI, where we show that substantial improvements in imaging resolution provide access to the quantum nature of the outgoing electron flux. The potential applications of photoionization are briefly mentioned in Sec. VII.

II. BASIC CONCEPTS OF PHOTOIONIZATION IN AN EXTERNAL FIELD

In this section, we summarize the fundamental peculiarities of classical electron trajectories in the presence of a Coulomb and a Stark field and the formation of the interference patterns. We introduce only the minimum of background necessary for understanding the experimental results presented later. A much more detailed analysis is available in our previous articles devoted to the classical [14] and semiclassical [15] description of photoionization in the presence of an external electric field. These articles largely rely on the seminal work of Demkov *et al.* [16] and Kondratovich and Ostrovsky [8–11], who discussed extensively the peculiarities of the classical motion of electrons under these conditions and introduced the principle of photodetachment and photoionization microscopy in the early 1980s. It is only very recently that the predictions of these authors have been confirmed experimentally, first in photodetachment [7] and next in photoionization [13].

Let us consider the ionization of a neutral atom in the presence of an external homogeneous electric field F. The principle of the experiment, as well as the definition of the axes and angles, is represented in Fig. 1. The combination of the Coulomb and Stark fields gives rise to the formation of a saddle point in the potential experienced by the electron at energy

$$E_{\mathrm{sp}} = -2\sqrt{F} \quad (\text{atomic units}). \tag{1}$$

The zero of the energy scale is defined as the field-free ionization limit. Above the saddle-point energy, the continuum is highly structured and exhibits quasidiscrete Stark resonances manifesting the presence of long-lived electron trajectories. The topology of the electron trajectories, and hence the pattern of impacts at large distance, depends only on the dimensionless reduced energy parameter $\varepsilon = E/|E_{\mathrm{sp}}|$. Note also that the classical motion of an electron in the combination of an attractive Coulomb field and a uniform electric field F directed along the z axis, and the problem of a hydrogen atom in an external electric field in quantum mechanics, are separable in parabolic coordinates [17,18]:

$$\xi = r + z, \quad \eta = r - z, \quad \varphi = \tan^{-1}(y/x). \tag{2}$$

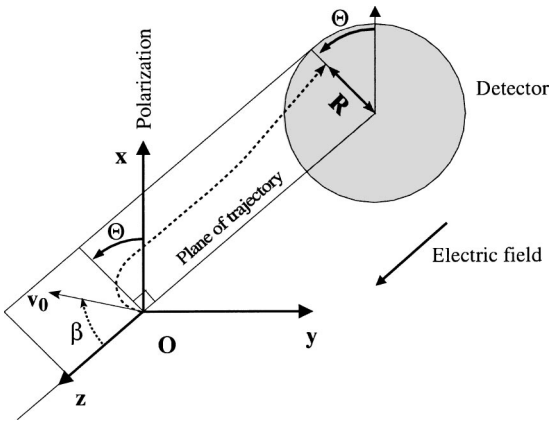

FIG. 1. Schematic view of the experimental arrangement used for photoionization microscopy. Photoization occurs at point O. The electric field is oriented along the z axis, perpendicular to the detector. The laser polarization is oriented along the x axis (unless explicitly mentioned in the text). The angle Θ between x axis and the plane of trajectory and the angle β between the initial velocity $\vec{\mathbf{v}}_0$ and the electric field are indicated.

One of the most important conclusions of the discussion of the classical motion [14] is the distinction between two different families of trajectories. The trajectories that never cross the field axis ($x=y=0$) are only weakly affected by the Coulomb field and are called direct since there is no rescattering of the ejected electron by the ionic core. All other trajectories are called indirect and involve a considerable extent of electron-core scattering. Remarkably, direct and indirect trajectories form two different structures in slow photoelectron images. Electrons following direct trajectories contribute to an inner circular structure, while those following indirect trajectories contribute to an outer concentric structure. In other words, direct trajectories are confined within a classical limit of radius R_I (see Fig. 2) and the accumulation of impacts at this radius leads to an inner ring in the image. Indirect trajectories are limited by the caustic surface that forms the boundary of the classically accessible region (radius R^c_{max}, also shown in Fig. 2).

The distinction between direct and indirect trajectories allows the introduction of an energy threshold E_{dir} that corresponds to the onset of direct trajectories. Below E_{dir} only indirect trajectories are allowed, while above E_{dir} direct trajectories exist for a limited range of ejection angles. The approximate expression of the direct ionization threshold is [15]

$$E_{\mathrm{dir}} \approx 0.775\, E_{\mathrm{sp}}. \tag{3}$$

We note that for excitation at energies just above E_{dir} electrons that are ejected in the direction of the saddle point

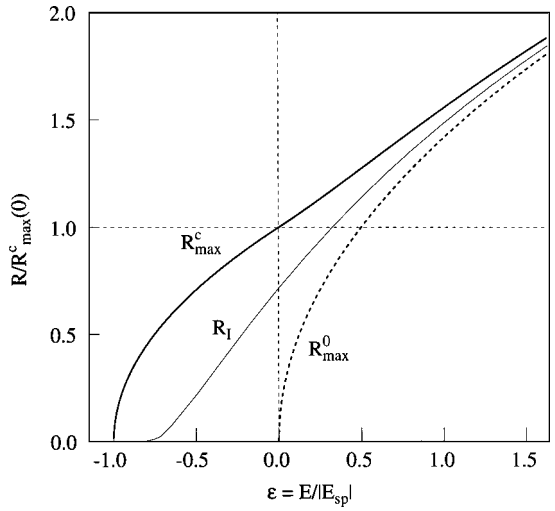

FIG. 2. Maximum radius of impact on the detector neglecting the Coulomb term $R^0_{\max}$ (dotted line) and taking the Coulomb term into account $R^c_{\max}$ (broad solid line) as a function of the reduced energy ε. At large ε values, $R^0_{\max}$ and $R^c_{\max}$ do not differ significantly while for $-1 \leqslant \varepsilon \leqslant 1$ the effect of the Coulomb interaction cannot be neglected. The radius R_I represent the maximum radius of impact for direct trajectories.

follow direct trajectories, whereas electrons that are emitted away from the saddle point follow indirect trajectories.

In summary, the analysis of classical trajectories allows us to distinguish four regions of energy (see Fig. 3): (1) below the saddle-point energy ($E < E_{\rm sp}$) the electron motion is bound; (2) for $E_{\rm sp} \leqslant E < E_{\rm dir}$ only indirect trajectories are allowed, which exhibit at least one crossing of the z axis; (3) for $E_{\rm dir} \leqslant E < 0$ direct and indirect trajectories coexist; (4) for $0 \leqslant E$ the motion is always open along the η coordinate. We point out that in cases 2 and 3 the motion is bound along ξ. It is furthermore bound along η if the angle β between the initial electron velocity and the electric field is smaller than the critical angle β_c, and open along η if $\beta \geqslant \beta_c$ with

$$\beta_c = 2 \arcsin\left(\frac{-E}{2\sqrt{F}}\right). \tag{4}$$

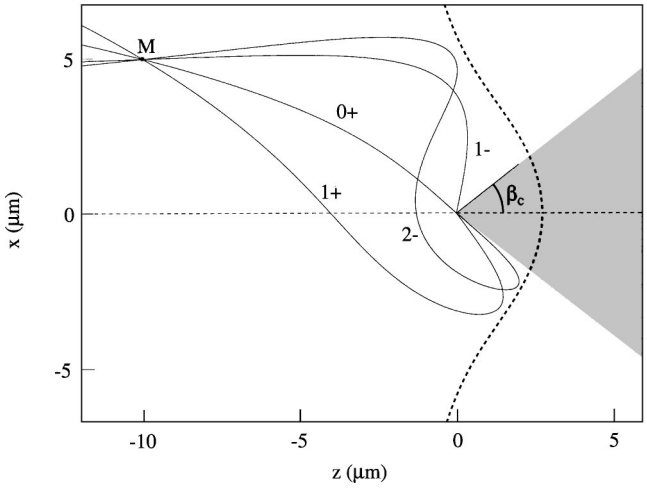

FIG. 3. Typical examples of classical trajectories leading to the same point M in a field $F = 1$ V/cm at an energy $E = -2$ cm^{-1}. The two direct trajectories, that do not cross the field axis (thin dashed line) are labeled 0^+ and 1^- (see text). Two selected indirect trajectories, which cross the field axis at least once, are shown (labels 1^+ and 2^-). The broad dashed line represents the equipotential limit separating the energetically accessible region (on the left) from the forbidden region (right). An electron launched at an angle smaller than β_c with respect to the electric field (gray shaded area) remains bound to the Coulomb center. Closed orbits are confined in the gray shaded area on the left side of the equipotential.

In the imaging of threshold photoelectrons the possibility arises for the observation of oscillatory patterns that can be interpreted as a manifestation of interferences among various classical trajectories. In photodetachment, only two trajectories interfere and the observed structures can easily be interpreted based on analytical expressions of the phase accumulated along both trajectories [7]. In the case of photoionization the trajectories are considerably more complex [15,9,19]. The simple parabolic trajectories relevant to photodetachment are strongly perturbed, due to the Coulomb interaction between the ejected electron and the residual ion, and one has to take into account the interference among an infinite number of classical paths. In the semiclassical approximation, the photoelectron wave function at a given point M of the detector may be represented as a sum of the contributions from all trajectories leading from the electron source to the point M. As opposed to the case of photodetachment, no simple analytical expression of the evolution of the fringe patterns with E and F can be derived. Therefore, a numerical evaluation of the various quantities has to be performed. This procedure is described in detail in Ref. [15] and allows us to calculate a radial probability distribution $P_{\rm calc}(R)$ that can be compared directly with the experimental radial probability distribution $P_{\rm expt}(R)$ defined as

$$P_{\rm expt}(R) = R \int P(R,\theta) d\theta, \tag{5}$$

where $P(R,\theta)$ represents the intensity distribution in the image in polar coordinates R and θ.

III. EXPERIMENT

The experimental setup is presented schematically in Fig. 4. In the experiment a beam of metastable Xe atoms was prepared by operating an electron impact source modeled after the design of Kohlhase and Kita [20] in a source chamber pumped by a 5200-l/s diffusion pump. A Xe atomic free-jet expansion was obtained by running a piezoelectric pulsed valve [21] with a 1-mm-diameter nozzle and an opening time of 200 μs in front of a 1-mm-diameter skimmer that was placed 5 cm downstream from the nozzle. This skimmer was mounted on a 12-cm-diameter circular plate in order to achieve a situation where Xe atoms emerging from the nozzle could reach the back side of the plate on the time scale of the experiment only by passing through the skimmer, rather than by passing around the plate. In this manner collimation of the Xe expansion was achieved without truly applying differential pumping. After the skimmer, the atoms

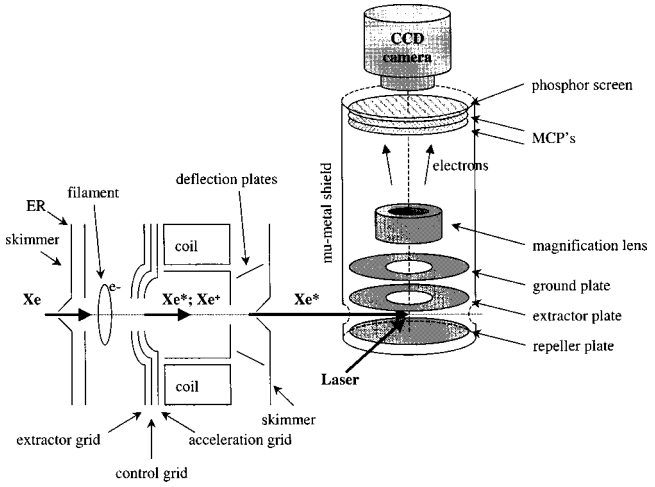

FIG. 4. Schematic view of the experimental setup. Metastable xenon atoms are produced in an electron impact source. They interact in the extraction region of the velocity-map imaging spectrometer with the ionization laser. Ejected electrons are projected onto a position-sensitive detector by the electric field.

passed through a filament made from a 2% thoriated tungsten wire with a diameter of 0.25 mm, wound into a coil that surrounded the atomic beam. The filament was typically operated at a current of 4 A. Electrons emitted from the filament were accelerated between a flat repeller plate with a 5-mm-diameter hole, typically operated at a voltage of −25 V, and a series of three hemispherical tungsten grids that were placed 3, 5, and 7 mm after the filament, and that were typically operated at 80, 160, and 240 V, respectively. The electrons were collected on two 20-mm-long cylindrically shaped anodes with a diameter of 1 cm that were formed from a stainless steel mesh and held at a voltage of 200 V. The anodes were placed inside a magnetic coil, consisting of 180 windings of 1.5-mm-diameter polyamide-covered copper wire around a 2-cm-inner-diameter aluminum cylinder. Under typical operating conditions, a significant increase in the production of metastable Xe atoms was observed when increasing the current in the coil, until saturation set in at a current of about 4 A. However, at this current the energy dissipation in the coil caused such an increase in the temperature of the piezoelectric pulsed valve that the valve shut down within one hour of operation. Therefore the coil was typically operated at a current of 1.5–2 A. After the coil, the atomic beam passed between two deflection plates operated at a potential difference of 180 V, which removed the majority of the electrons and ions from the beam. The metastable atom beam entered the central experimental chamber through a second skimmer with a diameter of 1 mm. The metastable Xe beam contained appreciable quantities of both the Xe $6s[3/2]_2$ metastable state at an energy of 67 068 cm^{-1} above the ground state and the Xe $6s'[1/2]_0$ metastable state at an energy of 76 197 cm^{-1} above the ground state. All experiments reported in this paper were carried out using the $6s[3/2]_2$ metastable state.

In the central experimental chamber, pumped by a 250-l/s turbomolecular pump, the metastable beam was crossed at right angles by the ionization laser. In most experiments this laser was a tunable 10-Hz pulsed dye laser (Lambda Physik Scanmate) with a bandwidth of 0.08 cm^{-1}. The laser was operated using DCM dye. Either the fundamental output of the dye laser was used to ionize the metastable Xe atoms via a two-photon process (using typically 4 mJ/pulse), or the frequency-doubled output was used in a one-photon process (using typically 0.1 mJ/pulse). In both cases the laser was focused onto the atomic beam using a 50-cm lens. The polarization of the laser was either along the direction of the electric field and perpendicular to the two-dimensional detector discussed below, or perpendicular to the electric field axis and parallel to the two-dimensional detector.

Photoelectrons resulting from the photoionization of metastable Xe atoms were detected using a velocity-map photoelectron detector similar to the original design of Eppink and Parker [2]. In this detector the acceleration of the electrons took place in two stages, first between a solid repeller plate and an extractor plate with a 20-mm hole, and next between this repeller plate and a ground plate with a 20-mm hole, which formed the entrance to a 47-cm-long field-free flight tube. At the end of the flight tube a dual microchannel plate (MCP) + phosphor screen assembly (F2226-24PX, Hamamatsu Photonics) was mounted and a charge-coupled device (CCD) camera (Pulnix, TM-9701) was used to record the 2D distribution of the light spots on the phosphor screen. Recorded images were transferred to a laboratory computer, where the images were accumulated after processing of the raw image by a peak-finding routine that determined the centroids of the observed spots on the phosphor screen [22]. This peak-finding routine was very important, since it provides a mechanism to completely get rid of CCD camera noise and furthermore improves the resolution of the acquired images. This latter aspect was important because in the first series of experiments to be reported here typical image sizes on the phosphor screen were only 1–2 mm, whereas the diameter of a single light spot on the phosphor screen can easily be several hundred micrometers. Of course, a successful implementation of the peak-finding routine required that the detected signals be kept rather low, in order to avoid the occurrence of overlapping electron spots. Typical operating voltages of the repeller and extractor electrodes were −1300 and −1010 V, respectively. In order to shield against the earth magnetic field and magnetic fields generated in the metastable source, the detector assembly was surrounded by one layer of μ-metal. In order to suppress the detection of electrons originating from the metastable source, the MCP was operated with a 100-ns gate, during which the voltage applied to the back of the MCP was raised from 1 kV to the nominal operating voltage of 1.8 kV. The back of the MCP and the phosphor screen were capacitively coupled, in order to maintain the 3 kV voltage differential between the back of the MCP and the phosphor screen during the voltage pulse applied to the MCP.

The velocity-map imaging detector described above was used in the first series of experiments reported in this paper, which concentrate on the distinction between direct and indirect ionization processes. In a second series of experiments, concerned with the appearance of interference fringes in the photoelectron images, a magnifying Einzel lens was

incorporated in the detector assembly [6]. This lens allowed a magnification of the photoelectron image on the detector by as much as a factor of 20. In this case, the repeller and extractor voltages were operated in a manner where a velocity-map image of the asymptotic velocity distribution was formed halfway in the field-free flight tube on the input side of the Einzel lens, and this distribution was subsequently imaged onto the MCP detector. The magnification provided by the Einzel lens allowed near-complete resolution of the interferences which occur between different electron trajectories, and furthermore allowed us to obtain high-quality images even when applying significantly higher voltages to the repeller and the extractor, where the images without the lens would otherwise be too small.

When using the magnifying lens, the alignment of the velocity-map imaging geometry was found to be very critical. When small errors exist in the alignment of the extraction electrodes with respect to the axis of the detector defined by the Einzel lens, a magnified image is formed away from the center of the microchannel plate detector and distortions are observed in the images. When the alignment is correct, operation of the Einzel lens does not move the center of the image on the imaging detector and high-quality images are observed.

IV. FROM VELOCITY-MAP IMAGING TO SLOW PHOTOELECTRON IMAGING

Two-dimensional photoion/photoelectron imaging was developed in the last 15 years as a method to measure kinetic energy and angular distributions for electron and ions resulting from photoionization and photodissociation events or chemical reactions [1,23]. In its most common form, depicted schematically in Fig. 1, the method consists of measuring a two-dimensional projection of the three-dimensional velocity distribution by accelerating the electrons or ions toward a two-dimensional detector where the positions of the electron or ion impacts are measured. If one makes sure that the experiment contains an axis of cylindrical symmetry parallel to the detection plane, then the three-dimensional velocity distribution can be recovered from the measured two-dimensional distribution by using a mathematical inversion technique [24–26]. Typically, the measured two-dimensional distributions consist of a number of concentric rings, where each ring corresponds to a particular kinetic energy of the ejected electrons or ions. These rings arise due to the fact that the Jacobian for the transformation from velocity space to position contains a singularity for ejection of the particles perpendicular to the detector axis. The filling pattern of the rings is determined by the angular distribution of the ejected particles.

The results of two-dimensional imaging experiments change dramatically when slow photoelectrons resulting from the photoionization of neutral atoms or molecules are detected [12]. In Fig. 5 a series of photoelectron images are shown that were recorded for two-photon ionization of metastable Xe $6s[3/2]_2$ atoms near the ionization threshold, by using a tunable laser at a number of wavelengths near 650 nm. The electric field value was set to F $=170$ V/cm ($E_{sp}\approx -79.8$ cm^{-1}). In the experiment the energy of the metastable state, the ionization potential of the atom, the energy of the saddle point in the effective potential experienced by the electron due the electric field of the velocity-map imaging detector, and the photon energy are all known to subwavenumber accuracy, and hence the kinetic energy of the ejected photoelectrons is known with this same precision. Nevertheless, as can be seen, for example, in the image recorded at $E=-35.3$ cm^{-1}, the photoelectron image contains a weak outer ring, a stronger inner ring, and a peak in the center of the image, as if photoelectrons were formed with at least three different kinetic energies.

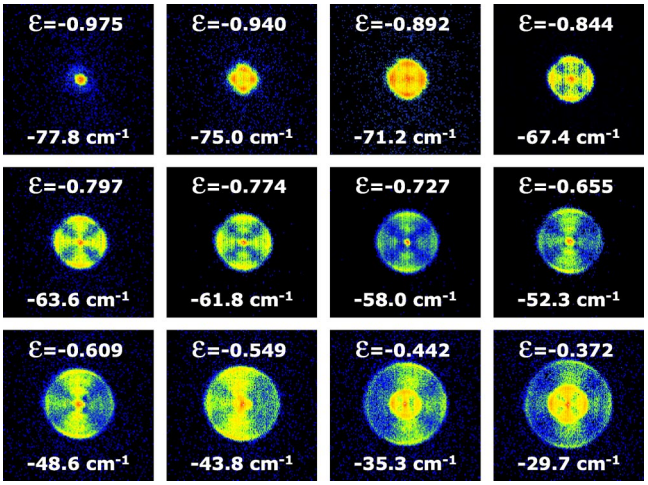

FIG. 5. (Color online) Photoelectron images recorded for two-photon ionization of metastable Xe $6s[3/2]_2$ atoms above the saddle point in an electric field $F=170$ V/cm. Energies relative to the zero-field ionization threshold, as well as reduced energies, are indicated. The laser polarization is oriented parallel to the detector along the vertical axis.

In order to follow the evolution of these multiple ring structures, images were recorded at a large number of excitation wavelengths, as shown in Fig. 5. In this figure the long-wavelength limit ($E=-77.8$ cm^{-1}) corresponds to excitation of the atom just above the saddle point in the effective potential experienced by the electron (reduced energy ε $=E/2\sqrt{F}\approx -0.975$), where the photoelectron is formed with little initial kinetic energy, so a small spot is observed on the detector. When the photon energy is increased, the photoelectron is formed with a small excess kinetic energy, and—as expected—the dot expands to a ring. However, the observed image is different from the image expected in conventional velocity-map imaging: a dot remains visible in the center of the image and the radius of the ring remains below the value expected on the basis of the excess kinetic energy, the field strength, and the electron optics geometry. We note that the crosslike pattern in the images is due to the fact that ionization occurs by means of two-photon excitation.

When the energy is further increased, further qualitative changes occur in the images. Near $\varepsilon=-0.66$ two relatively weak rings are visible between the central dot and the brighter ring at the outer limit of the image, and near $\varepsilon=$ -0.55 the image undergoes a rapid and dramatic change in appearance. The intensity in the center of the image rapidly

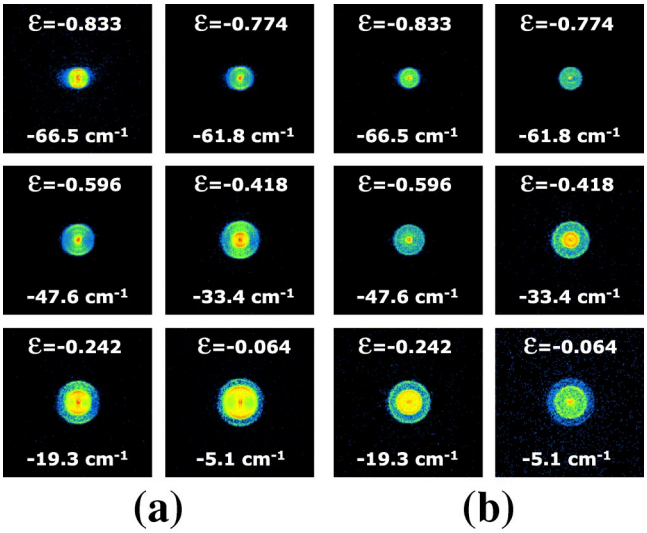

FIG. 6. (Color online) Photoelectron images recorded for one-photon ionization near 325 nm of metastable Xe $6s[3/2]_2$ atoms above the saddle point in an electric field $F=170$ V/cm. Laser polarization (a) parallel to the detector along the vertical axis and (b) perpendicular to the plane of the detector.

increases at the expense of the outer ring, which is almost completely gone at $\varepsilon=-0.37$, and the central dot expands to a ring similar to the one that was observed near the saddle point. At even higher energy the central dot slowly decreases in intensity relative to the new outer ring and asymptotically the image approaches the "normal" velocity-map image, displaying a single ring with a radius determined by the kinetic energy of the ejected electrons.

The main aspects of the evolution of the photoelectron images as a function of wavelength on excess energy, namely, (1) the formation of a ring with a central dot near the saddle point, (2) the increase in intensity of the central dot at the expense of the outer ring near a reduced energy $\varepsilon=-0.5$, (3) the subsequent disappearance of the outer ring and the expansion of the central dot into a new ring, and (4) the observation of weak additional rings between the central dot and the bright outer ring of the image, are robust with respect to changes in the laser polarization, laser wavelength (one-photon ionization versus two-photon ionization), and electric field strength. An example is shown in Fig. 6, where images are shown for one-photon ionization of metastable Xe $6s[3/2]_2$ atoms at six wavelengths near 325 nm, with the laser polarization either parallel to the plane of the detector (perpendicular to the electric field of the imaging spectrometer), or perpendicular to the plane of the detector (parallel to the electric field of the imaging spectrometer). While the filling patterns of the observable rings depend on the laser polarization (revealing a preference for ionization along the laser polarization axis in the former case and an isotropic angular pattern in the latter case), the main features in both measurements are very similar, and moreover very similar to the images shown in Fig. 5 In particular, between $\varepsilon=-0.60$ and -0.42, the central dot rapidly grows in intensity at the expense of the outer ring, and itself expands into a ring.

The main trends observed in Figs. 5 and 6 can conveniently be displayed in a contour plot showing the radial

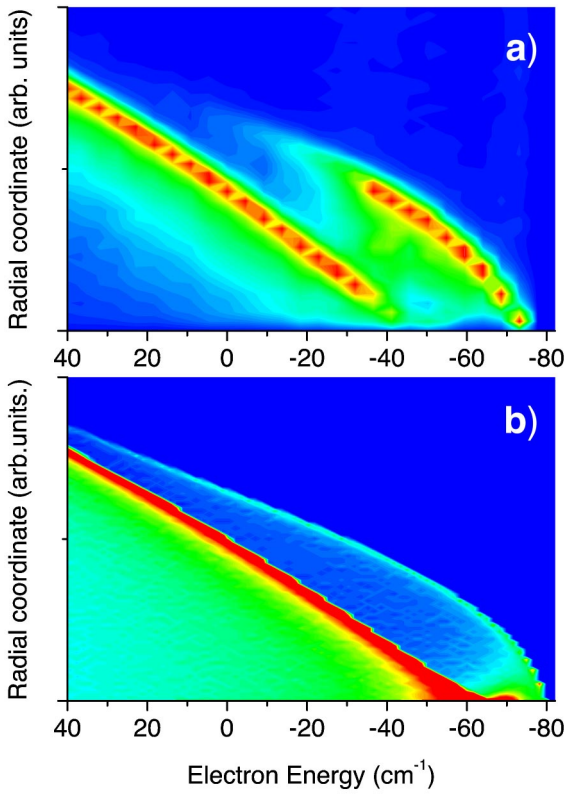

FIG. 7. (Color online) Contour plot showing the radial distribution of the images as a function of excitation laser wavelength. (a) Experimental results for one-photon ionization with the laser polarization parallel to the plane of the detector. The radius of the image increases with increasing energy until the intensity in the ring suddenly drops near $E\approx-35$ cm^{-1} and is shifted to the inner part of the image. At higher energies the inner part of the image expands to a ring similar to the ring that was observed immediately above the saddle point. (b) Result of a classical simulation where the density of electrons impacting on the position-sensitive detector at a given radius has been included in a representation similar to Fig. 2.

distribution of the images as a function of the electron kinetic energy. In Fig. 7(a) this contour plot is shown for the experiment performed using one-photon ionization with the laser polarization parallel to the plane of the detector. From the saddle point ($E\approx-80$ cm^{-1}, i.e., $\varepsilon\approx-1$) the radius of the image increases with increasing energy, until the intensity in the ring suddenly drops near $E\approx-35$ cm^{-1}($\varepsilon\approx-0.45$) and is shifted to the inner part of the image. For higher energies this inner part of the image expands to a ring similar to the ring that was observed immediately above the saddle point. The radius of the second ring initially stays below the value expected based on the photoelectron kinetic energy, the electron optics geometry, and the applied voltages, but asymptotically ($\varepsilon\gg1$) approaches this value when the conventional regime of velocity-map imaging is entered.

The classical trajectories that were discussed in Sec. II provide the basis for an interpretation of the observations in Figs. 5, 6(a), 6(b), and 7(a). In Fig. 7(b) a contour plot is shown that was determined by calculating the projection of photoelectrons that are ejected with an isotropic angular distribution with respect to the laser polarization axis onto a flat

screen placed in the asymptotic region of the ionization process, where the spatial distribution reflects the electron velocity distribution in a plane perpendicular to the detector axis. The latter represents the velocity distribution that is mapped onto the two-dimensional detector by the velocity-map electron imaging optics. The contour plot was generated by calculating the projections as a function of the kinetic energy of the photoelectrons at the saddle point in the effective potential experienced by the electron. Figure 7(b) is very similar to Fig. 2 presenting the maximum radius of impact of both kinds of trajectories, with the additional information in Fig. 7 about the quantity of trajectories accumulating at the relevant maximum radius. Consistent with the analytical treatment given in the previous section, direct trajectories appear in Fig. 7(b) only for $E > E_{\mathrm{dir}} = 0.755 E_{\mathrm{sp}}$. A comparison of the experimental contour plot shown in Fig. 7(a) and the simulated contour plot shown in Fig. 7(b) illustrates that the appearance of two branches in the experimental contour plot can be understood on the basis of purely classical arguments. Inspection of the photoelectron trajectories shows that near threshold ($-1 < \varepsilon < -0.7$) the ionization is dominated by indirect trajectories where the electron is scattered by the core and crosses the detector axis at least once before reaching the detection plane (i.e., one or several zeros in the parabolic coordinate ξ). By contrast, at higher energies the ionization is dominated by direct trajectories where the electron reaches the detection plane without crossing the detector axis. This evolution in the photoelectron trajectories as a function of the excess energy with respect to the saddle point in the effective potential is highly intuitive. In the absence of any external electric field the potential experienced by the electron is purely Coulomb. The presence of the dc electric field introduces a term $-Ez \cos \beta$ that leads to the formation of a saddle point along the direction of the electric field. For a given energy E above the saddle point photoelectrons can escape directly toward the detection plane if the angle β with respect to the electric field (see Fig. 1) lies above a maximum angle $\beta_0(E)$ (see Fig. 5 of Ref. [1]). At the saddle point ($\varepsilon = -1$), $\beta_0(E)$ is equal to π, whereas $\beta_0(E)$ decreases to 0 for large kinetic energies ($\varepsilon \gg 1$). For ejection angles between the critical angle $\beta_c(E)$ [Eq. (4)] and $\beta_0(E)$, the photoelectrons encounter an outer turning point in the effective potential and interact one or more times with the ion before they manage to find the hole in the effective potential and escape through it. In other words, repeated encounters between the electron and the ion alter the electron trajectory in such a fashion that eventually the electron approaches the hole in the effective potential at an angle with the electric field axis which lies above the maximum angle $\beta_0(E)$. When the kinetic energy of the photoelectrons increases, the value of $\beta_0(E)$ decreases and a larger and larger fraction of the electrons escape the effective potential following a direct trajectory, where no further interactions with the ion take place.

The comparison between the experimental and calculated contour plots in Fig. 7 is only approximate. In the classical theory electrons remain bound to the ion indefinitely if they are ejected at an angle below the critical angle β_c. This behavior does not persist in quantum mechanics, and as a result the experimental contour plot shows a smooth evolution of the total integrated intensity as a function of wavelength, whereas the classical calculations show a major drop in the integrated intensity of the image as the wavelength approaches the saddle point. Importantly, however, this does not change the appearance of the contour plots qualitatively.

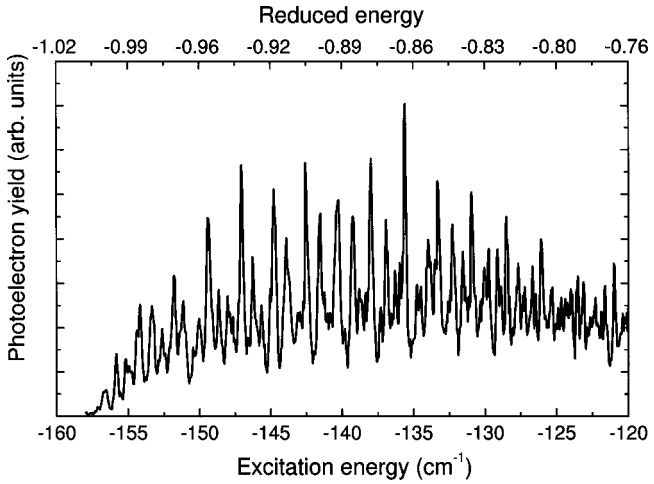

FIG. 8. Example of continuum Stark structure above the saddle point for excitation of metastable Xe $6s[3/2]_2$ in a dc electric field of approximately 650 V/cm. The photoionization efficiency curve shows numerous resonances. Well-defined quantum numbers cannot be attributed to these resonances in the general nonhydrogenic case.

V. STARK-STATE-RESOLVED SLOW PHOTOELECTRON IMAGING

In the previous section the appearance of direct and indirect ionization processes was discussed as a function of the kinetic energy of the ejected photoelectrons with respect to the saddle point in the effective potential experienced by the electron. In this discussion we ignored the fact that in the continuum above the saddle point a continuation of the electric-field-induced Stark structure exists. In the case of the hydrogen atom, there is a one-to-one connection between the parabolic quantum numbers describing a particular continuum Stark state and localization of the electron wave function on the effective potential. So-called blue Stark states are localized in the uphill direction of the effective potential and increase in energy when the magnitude of the electric field is increased, whereas so-called red Stark states are localized in the downhill direction of the effective potential and decrease in energy when the magnitude of the electric field is increased. It is an interesting question to investigate whether one can selectively eject the photoelectron along a specific type of trajectory by tuning onto an appropriate continuum Stark resonance, In order to investigate the possibility of this selectivity, experiments were carried out at larger electric field strengths, where the density of continuum Stark states was low enough to be resolved by the dye laser used. Adequate imaging resolution was maintained in these experiments by making use of the magnification Einzel lens discussed in the experimental section.

In Fig. 8 an example is shown of the continuum Stark structure above the saddle point to ionization for excitation

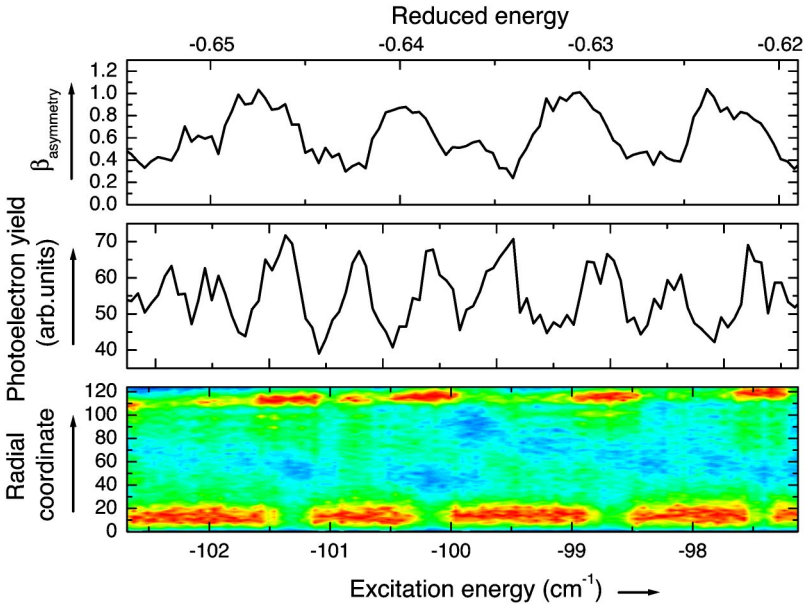

FIG. 9. (Color online) A small portion of the Xe photoionization spectrum near the onset of the direct ionization channel ($F \approx 650$ V/cm). From top to bottom: asymmetry parameter (coefficient of the second Legendre polynomial in the equation of the photoionization cross section) as a function of the energy relative to the zero-field ionization threshold; photoionization efficiency curve showing a number of continuum Stark resonances; contour plot of the radial distribution of the photoelectron image.

of metastable Xe $6s[3/2]_2$ in a dc electric field of approximately 650 V/cm. The photoionization efficiency curve shows numerous resonances, which result from a continuation of the Stark structure into the continuum. Assignment of the individual resonances that appear in the spectrum is a daunting task. Since the quantum defects for p -and d-type orbitals are large in xenon, Stark levels repel each other very strongly near the numerous crossings that occur beyond the Inglis-Teller limit, resulting in a significant loss of regularity in the spectrum. As a result, although visual inspection suggests the presence of a number of overlapping Stark manifolds with principal quantum numbers in the range between 25 and 30, we have been unable to connect the observed levels with positions based on the calculation of a Stark map using an effective Hamiltonian approach [27]. Nevertheless, the observation of resolved continuum Stark states does allow us to investigate to what extent the observation of direct and indirect trajectories—as discussed in the previous section—is connected to the excitation of continuum Stark resonances by the laser.

In Fig. 9 a small portion of the Xe photoionization efficiency curve is shown for excitation of metastable Xe $6s[3/2]_2$, near the onset of the direct ionization channel ($\varepsilon \approx 0.64$), again employing an electric field of approximately 650 V/cm. As shown in the central part of Fig. 9, a number of continuum Stark resonances can clearly be discerned in this portion of the spectrum. Direct ionization shows up as a contribution in the center of the photoelectron image, while indirect ionization shows up as a ring surrounding this center. Therefore the dependence of the direct and indirect photoionization can be evaluated from a contour plot, where the radial distribution of the photoelectron image is plotted as a function of the photoelectron kinetic energy with respect to the saddle point. In the lower part of Fig. 9, a correlation between indirect ionization and excitation of a continuum Stark resonance can be clearly observed. Substantial indirect ionization is observed only at four regularly spaced positions in the spectrum, which coincide with the positions of four peaks in the photoionization efficiency curve, However, there are clearly more peaks in the photoionization efficiency curve than positions where enhancement of the indirect ionization channel occurs. This suggests that individual continuum Stark resonances display different branching ratios for direct versus indirect ionization, and agrees with the notion that laser excitation of continuum Stark states leads to the formation of an electron wave packet with a certain degree of localization on the effective potential surface that determines its subsequent decay. It is likely that the observed differences in the branching ratios between direct and indirect ionization are correlated with the lifetimes of the continuum Stark states. This correlation could be further investigated using a high-resolution laser source.

When the laser wavelength is tuned, interesting changes also occur in the angular distributions with respect to the laser polarization axis. The asymmetry parameter ($\beta_{\text{asymmetry}}$) that describes the angular distribution gradually increases from approximately zero near the saddle point to positive values at higher excitation energies (i.e., preferential photoelectron emission parallel to the laser polarization axis). However, the asymmetry parameter displays rapid variations as a function of energy. In the upper part of Fig. 9 the asymmetry parameter for the outer portion of the photoelectron images (corresponding to the indirect ionization component) is shown as a function of the energy. Substantial changes occur in the asymmetry parameter, which, moreover, are correlated with the observed continuum Stark resonances. At the four peaks in the photoionization efficiency curve where enhanced indirect ionization is observed, the asymmetry parameter likewise reaches a maximum value. The observed correlation between the value of the asymmetry parameter and the occurrence of an enhanced indirect ionization again underscores the importance of continuum Stark resonances in the photoionization dynamics. In the experiment the photoexcitation leads to the formation of an electron wave packet that either is directly in the continuum or corresponds to a quasibound Stark resonance. Our experiment shows that the excited continuum electron wave functions are qualita-

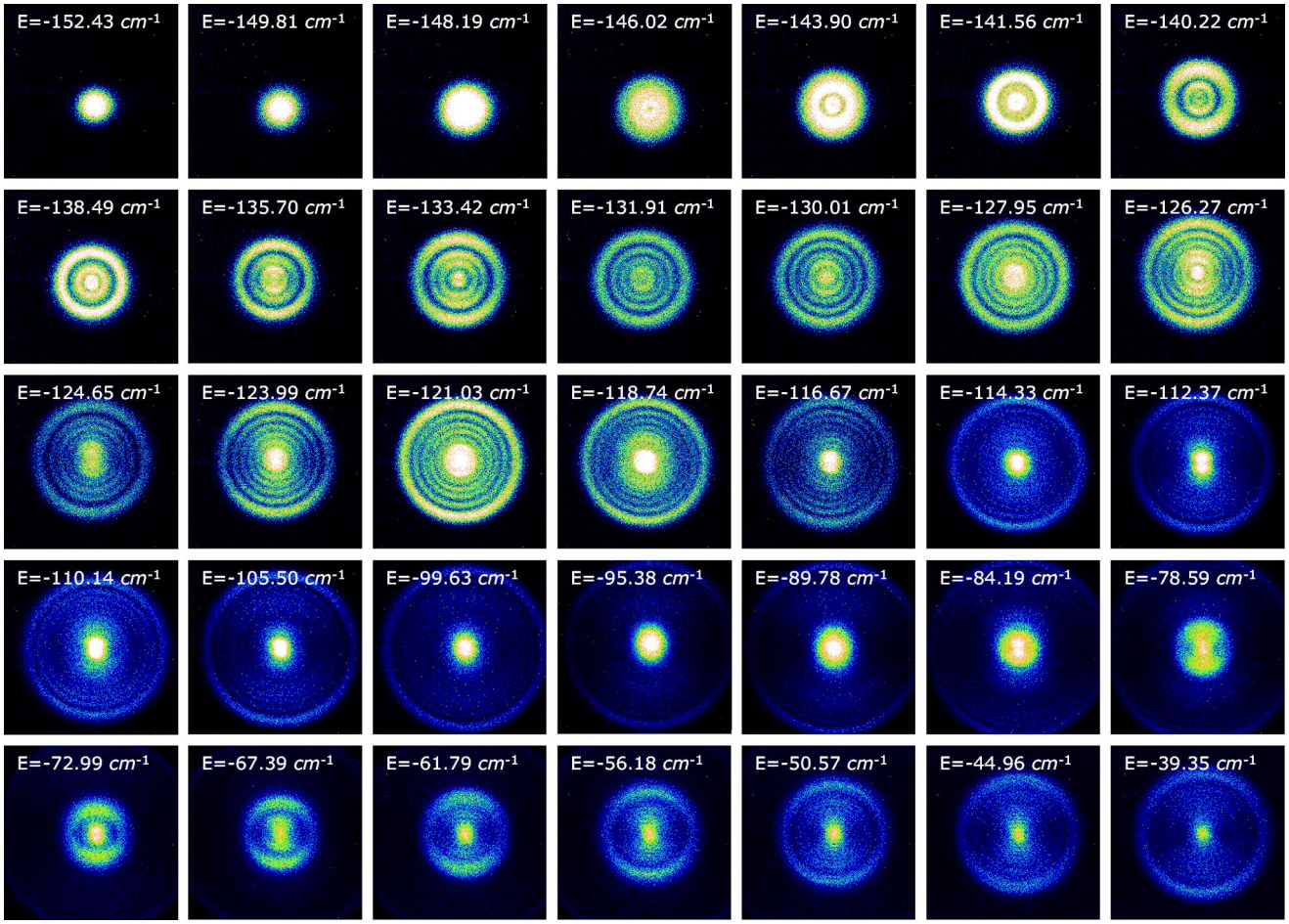

FIG. 10. (Color online) Overview of photoelectron images recorded at $F=615$ V/cm. The energy increases from the saddle point (top left) up to just below the zero-field ionization threshold (bottom right). The onset of direct trajectories appears at about $E=-117$ cm^{-1}, where the intensity of the central peak becomes significantly larger than the outer ring.

tively different from the continuum Stark wave functions, so that the photoexcitation efficiency, the initial localization of the electron wave function, the branching between indirect and direct ionization, and the angular distribution of the indirect ionization component depend in a consistent manner on whether or not a continuum Stark resonance is excited by the laser.

As discussed, the assignment of the various resonances observed in the continuum is not performed at this point. A standard perturbative treatment and an effective Hamiltonian approach are unable to quantitatively analyze these structures, which require using a generalized multichannel quantum defect treatment [28]. Interestingly, though, the next section will show that interference structures that appear in the images at high resolution can be understood using a semiclassical approach, i.e., without precise knowledge of the detailed nature of every resonance.

VI. PHOTOIONIZATION MICROSCOPY

In the present section, we will concentrate on the additional physics that can be accessed when doing slow photoelectron imaging at an image resolution that allows distinguishing the quantum nature of the outgoing electron flux, In Sec. IV, slow photoelectron imaging was presented under conditions where the instrumental resolution allows distinguishing contributions corresponding to direct and indirect ionization in the classical envelope of the outgoing electron current. By simply inserting a magnification lens as described in Sec. III, it is possible to reach a resolution sufficient to observe modulation in the electron image originating entirely from the quantum nature of the problem. The results presented in the following have been obtained under experimental conditions allowing us to achieve simultaneously spectral resolution (i.e., Stark-state-resolved imaging) and geometrical resolution (i.e., a limited number of fringes in the experimental images). According to the semiclassical model [15] both conditions may be satisfied when working at rather high field values. Because it reveals the quantum aspects of the outgoing electron current, we have called this kind of imaging "photoionization microscopy."

Figure 10 shows representative examples from a series of more than 200 images that were taken in an external electric field of 615 V/cm by scanning the excitation energy above the saddle point. These are raw images and neither filtering nor symmetrization has been applied. Images were recorded both on continuum Stark resonances, and in between reso-

nances. Here and in the following the laser excitation involved one-photon excitation using tunable uv light and the laser polarization was parallel to the plane of detection and oriented along the vertical axis.

All the features described above regarding slow photoelectron imaging are clearly seen in this series of images where, in addition, the quantum nature of the electron current becomes visible thanks to the use of the magnification lens. The first image of the series presented in Fig. 10 (top left) corresponds to tunnel ionization, about 0.6 cm^{-1} below the saddle point ($E_{sp}=-151.8$ cm^{-1}), in a region where classical trajectories are closed. When the excitation energy increases (from left to right and from top to bottom) the classical envelope of electron trajectories increases in radius, as expected from a classical trajectories simulation, but, in addition, a clear modulation of this structure appears in the image about 10 cm^{-1} above the saddle-point energy. When the energy is increased further, the oscillating structure develops and an increasing number of fringes appear. The most striking feature of this fringe pattern is its totally smooth evolution and the regular increase of the number of fringes, irrespective of being on or off resonance. When the onset of direct trajectories is reached ($E_{dir}\approx-117.7$ cm^{-1}), the intensity of the central spot increases significantly as compared to the rest of the image. This is due to the fact that direct trajectories become allowed and, as shown by classical simulations [14], they initially contribute at very small impact radius. As the energy is increased further above this second threshold, the contribution from direct trajectories increases slowly in size and develops its own system of fringes which is incommensurate with the fringe pattern arising from indirect trajectories. As a consequence, a beating pattern appears in the central part of the images, where both direct and indirect trajectories are detected. This is visible in the last images of the series presented in Fig. 10 in the region 40–60 cm^{-1} below the zero-field ionization threshold.

The interference between direct and indirect trajectories is even clearer in the images presented in Fig. 11 which correspond to a very long accumulation time (10 000 laser shots) in order to improve the signal-to-noise ratio. In that case, the electric field value is set to $F=320$ V/cm. Even though the details are not totally resolved, owing to the large number of fringes, the onset of central structure corresponding to direct trajectories is obvious in the top left image, and its progressively increasing contribution, which rapidly becomes dominant, is also clearly visible. The beating structure in the inner component is particularly visible in the bottom left image, precisely in a region where both direct and indirect contributions are of comparable magnitude.

Another distinctive feature observed above E_{dir}, which was already clearly seen in previous slow photoelectron imaging experiments, is the appearance of a very strong photoelectron peak in the center of the image at radius $R=0$. It arises straightforwardly from the classical simulations. When the Coulomb field is neglected, only electron trajectories launched at angle $\beta=0$ or $\beta=\pi$ contribute at $R=0$. On the contrary, when the Coulomb field is taken into account, there exist many other angles of ejection leading to $R=0$ [14]. Since the number of classical trajectories is proportional to the solid angle, and hence proportional to $\sin\beta$, the contribution at $R=0$ dramatically increases when trajectories with $\beta\neq0$ or π reach the center of the image, leading to the formation of an intense peak there. Although this feature appears significantly below E_{dir}, and persists at positive energy well above $|E_{sp}|$, it is especially prominent when direct trajectories contribute to the image formation. Naturally, this feature, a manifestation of the long-range interaction, is totally absent in photodetachment. In the present case, the shape of the potential surface close to the saddle point really provides a lens effect that refocuses the divergent electron flux. It is an intriguing thought to consider whether the enhanced flux density that results at the center of the detector could be used advantageously in electron microscopy.

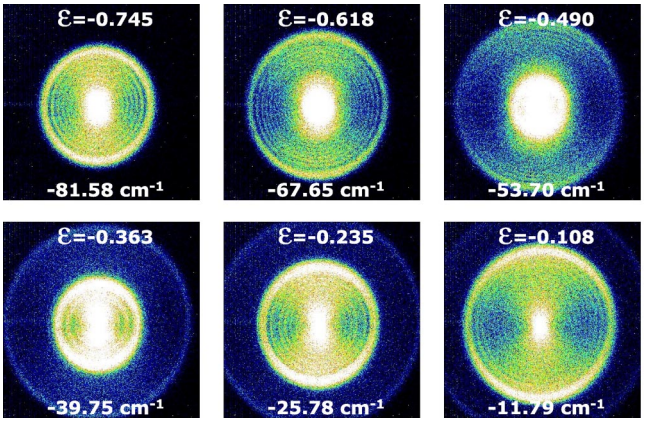

FIG. 11. (Color online) High-resolution photoelectron images recorded at $F=320$ V/cm. The onset of direct trajectories is clearly visible as a second, inner, system of fringes tht enlarges and becomes more and more intense as energy increases. The beating pattern between direct and indirect contributions is also visible in the lowest images, particularly at $\varepsilon=-0.363$, where both contributions are of comparable magnitude.

The smooth evolution of the fringe pattern, combined with its apparent very weak dependence on the resonance or continuum nature of the spectral range optically excited, is a strong indication that major features observed in the interference pattern are not due to the resonant character of the excited transition. Therefore, it is strong support for the assumptions made in our semiclassical description [15]. Among these, we assume a constant weight for all classical trajectories in the calculation of the semiclassical wave function (*s* wave). The good agreement between experimental results and simulations based on that approximation further justifies this crude assumption. On the basis of this hypothesis, semiclassical simulations of the fringe pattern were performed following the approach summarized in Sec. II. In the present article, which deals mostly with experimental results, we limit the presentation of this comparison to a single image but a more extensive comparison is available in Ref. 15. Figure 12 (left) presents a typical image obtained in a field $F=615$ V/cm, at an energy $E=-127.95$ cm^{-1} ($\varepsilon=-0.843$). The image clearly exhibits four bright fringes and a very intense component in the center. A comparison of the experimental (broad solid line) and calculated (thin solid line) radial distributions [see Eq. (5)] is presented on the right-hand side of the figure. The fringe positions are in extremely good

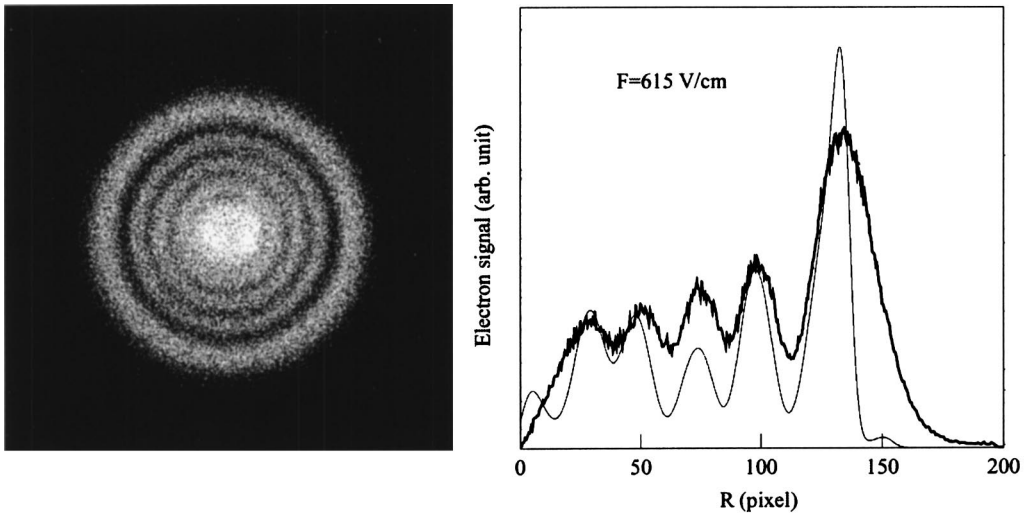

FIG. 12. Typical image recorded in a field $F=615$ V/cm, at energy $E=-127.95$ cm^{-1} ($\varepsilon=-0.843$). Left: experimental image; right: comparison of the experimental (broad solid line) and theoretical (thin solid line) radial probability distributions $f(R)$.

agreement. The variations of the relative intensity of the various fringes as well as the fringe contrast are more pronounced in the numerical simulation. This is partly due to the finite resolution of both the excitation laser and the photoelectron spectrometer, but also to the approximations made in our model. Another strong approximation of the semiclassical model also appears clearly in the comparison shown in Fig. 12. The semiclassical approximation fails whenever a zero is encountered in the momentum along one of the parabolic coordinates. This happens in particular at the caustic surface and is at the origin of the noticeable discrepancy observed at the outer edge of the radial distribution. The external fringe is found to be much broader in the experiment than in the simulation: the effective electron current extends significantly beyond the classically accessible region. The semiclassical simulation presented in Fig. 12 involves in fact some averaging. The "exact" classical result essentially has a vertical cutoff at the maximum radius. Of course, a full quantum treatment of the problem would remedy this discrepancy.

An important question that arises from the observation of a very regular progression of the interference patterns as a function of energy is the influence of the nonhydrogenic character on that surprisingly simple behavior. Indeed, in the case of atomic hydrogen, we would expect a nonmonotonic evolution of the fringe pattern in the images. On narrow resonances that correspond to a well-defined value of the parabolic quantum number n_1 [17,18], we would expect to observe n_1 dark fringes, this parabolic quantum number being precisely the number of nodes of the wave function along the coordinate ξ. Since the various manifolds of different principal quantum number n are totally overlapping in the region of interest, well above the Inglis-Teller limit, the number of nodes is thus expected to vary rather erratically from one resonance to another. Off resonance, however, the interferogram is expected to be dominated by the so-called background contribution introduced by Kondratovich and Ostrovsky [8–11] which has a rather smooth evolution. Despite the clarity of the present results, it is nevertheless not totally clear that such a difference between excitation on or off resonance would be observable in atomic hydrogen. Therefore, we aim to repeat the present experiments in atomic hydrogen. In the present case of a nonhydrogenic system, the smooth evolution of the fringe pattern as a function of energy can be rationalized by considering that the mixing among all Stark states is very strong and, although every resonance in the continuum is exactly connected to a given parabolic quantum number at moderate field strengths, the large number of anticrossings in the continuous spectrum implies that the wave function is somehow averaged over all quantum numbers and is therefore only slightly dependent on the resonant character of the excited transition.

VII. CONCLUSION AND PERSPECTIVES

In this article we have presented the major results that we have obtained in slow photoelectron imaging and photoionization microscopy in atomic xenon. A classical or semiclassical model has been used and has allowed a detailed interpretation of the observed features in slow photoelectron imaging and in microscopy, respectively. Using standard velocity-map imaging at its limit has proven to be very efficient for observing the main influence of the presence of the Coulomb field on classical trajectories of the electrons. We have shown that some information regarding the localization of the wave function at a given Stark resonance may be inferred from the relative intensities of the direct and indirect ionization contributions in the image of low-kinetic-energy electrons. By improving the resolution of our apparatus, the quantum nature of the outgoing electron current has been observed and has subsequently been interpreted in terms of interferences among classical trajectories leading from the atom to a given point on the detector. A very good agreement between our experimental results and the semiclassical simulation has been obtained, using only very simple approximations. Somewhat surprisingly, the interference patterns that mirror the transverse component of the wave function exhibit a very smooth evolution with energy that is apparently con-

nected to the high degree of n mixing in the continuum Stark spectrum. From this point of view, a clarification of our general understanding of the relevant processes is expected from the observation of photoionization microscopy in atomic hydrogen.

In addition to this additional experimental work, related theoretical effort is necessary. In order to go beyond the intrinsic limitations of the semiclassical model we have to develop a full quantum treatment of that problem. Although it is a rather heavy development, the generalized formulation of the multichannel quantum-defect theory [28] allows in principle a detailed representation of excited Rydberg states coupled to the ionization continuum in an external electric field.

Similar to the case of photodetachment microscopy [7], photoionization microscopy can be used as a tool for performing high-precision measurements of ionization thresholds. However, in the case of photoionization, it is probably not competitive with the extrapolation of Rydberg series. Rather, photoionization microscopy may be used as a test of fundamental concepts or problems. Being an interferometric method, photoionization microscopy is by nature extremely sensitive to any kind of perturbation that affects the electron trajectories. In this sense, photoionization microscopy provides an electronic interferometer with microscopic size. The sensitive part of the interferometer where the various trajectories followed by the electron may differ extends typically over one or a few micrometers, and it is precisely this small spatial extension that can allow stringent tests of some fundamental processes. The introduction of a magnetic field in the problem may lead to a wealth of additional phenomena like chaotic classical motion or the possibility of testing the Aharonov-Bohm effect [29], as suggested by Kondratovich and Ostrovsky in one of their articles [11].

Finally, interesting questions may be asked also regarding the time dependence of the interference pattern itself. In the classical picture, indirect electrons arrive on the detector significantly after the direct electrons. This has been observed explicitly in the picosecond domain by Lankhuijzen and Noordam [30] using a streak camera. These authors showed that when a Rydberg wave packet is excited above the saddle point, several recurrence peaks could be distinguished in the time-dependent ionization current that are related to direct ionization or multiple scattering of the electron by the ion. We could imagine a modification of the present experiment in order to time-resolve direct and indirect electrons and to look directly at the buildup of the interference pattern. In particular, the behavior of the beating pattern that results from the interferences between direct and indirect trajectories should disappear if a sufficiently high time resolution was available. This would provide an extremely spectacular and pedagogic example of the correspondence between quantum mechanics and a (semi)classical interpretation.

ACKNOWLEDGMENTS

This work is part of the research program of the "Stichting voor Fundamenteel Onderzoek der Materie (FOM)," which is financially supported by the "Nederlandse organisatie voor Wetenschappelijk Onderzoek (NWO)." It was furthermore supported by the "Van Gogh" program. We thank Dr. Florentina Rosca-Pruna, Dr. Marcel Warntjes, Dr. Herman Offerhaus, and Ingrid Sluimer for their help during parts of the experiment. The technical assistance of Hinco Schoenmaker and Rob Kemper is also gratefully acknowledged. C.N. acknowledges the EU for financial support. The research of F.L. is supported by EU RTN Network PICNIC (Grant No. HPRN-CT-2002-00183).

[1] D. W. Chandler and P. L. Houston, J. Chem. Phys. **87**, 1445 (1987).
[2] A. T. J. B. Eppink and D. H. Parker, Rev. Sci. Instrum. **68**, 3477 (1997).
[3] C. R. Gebhardt, T. P. Rakitzis, P. C. Samartzis, V. Ladopoulos, and T. N. Kitsopoulos, Rev. Sci. Instrum. **72**, 3848 (2001).
[4] D. Strasser, X. Urbain, H. B. Pedersen, N. Altstein, O. Heber, R. Wester, K. G. Bhushan, and D. Zajfman, Rev. Sci. Instrum. **71**, 3092 (2000).
[5] L. Dinu, A. T. J. B. Eppink, F. Rosca-Pruna, H. L. Offerhaus, W. J. van der Zande, and M. J. J. Vrakking, Rev. Sci. Instrum. **73**, 4206 (2002).
[6] H. L. Offerhaus, C. Nicole, F. Lépine, C. Bordas, F. Rosca-Pruna, and M. J. J. Vrakking, Rev. Sci. Instrum. **72**, 3245 (2001).
[7] C. Blondel, C. Delsart, and F. Dulieu, Phys. Rev. Lett. **77**, 3755 (1996).
[8] V. D. Kondratovich and V. N. Ostrovsky, J. Phys. B **17**, 1981 (1984).
[9] V. D. Kondratovich and V. N. Ostrovsky, J. Phys. B **17**, 2011 (1984).
[10] V. D. Kondratovich and V. N. Ostrovsky, J. Phys. B **23**, 21 (1990).
[11] V. D. Kondratovich and V. N. Ostrovsky, J. Phys. B **23**, 3785 (1990).
[12] C. Nicole, I. Sluimer, F. Rosca-Pruna, M. Warntjes, M. J. J. Vrakking, C. Bordas, F. Texier, and F. Robicheaux, Phys. Rev. Lett. **85**, 4024 (2000).
[13] C. Nicole, H. L. Offerhaus, M. J. J. Vrakking, F. Lépine, and Ch. Bordas, Phys. Rev. Lett. **88**, 133001 (2002).
[14] Ch. Bordas, Phys. Rev. A **58**, 400 (1998).
[15] C. Bordas, F. Lépine, C. Nicole, and M. J. J. Vrakkin, Phys. Rev. A **68**, 012709 (2003).
[16] Yu. N. Demkov, V. D. Kondratovich, and V. N. Ostrovsky, Pis'ma Zh. Eksp. Teor. Fiz. **34**, 425 (1981) [JETP Lett. **34**, 425 (1981)].
[17] H. A. Bethe and E. E. Salpeter, *Quantum Mechanics of One- and Two-Electron Atoms* (Springer, New York, 1957).
[18] L. D. Landau and E. M. Lifshitz, *Quantum Mechnics: Non-Relativistic Theory* (Addison-Wesley, Reading, MA, 1965).
[19] J. Gao and J. B. Delos, Phys. Rev. A **49**, 869 (1994).
[20] A. Kohlhase and S. Kita, Rev. Sci. Instrum. **57**, 2925 (1986).

[21] D. Proch and T. Trickl, Rev. Sci. Instrum. **60**, 713 (1989).
[22] B. Cahng, R. C. Hoetzlein, J. A. Mueller, J. D. Geiser, and P. L. Houston, Rev. Sci. Instrum. **69**, 1665 (1998).
[23] A. J. R. Heck and D. W. Chandler, Annu. Rev. Phys. Chem. **46**, 335 (1995).
[24] C. Bordas, F. Paulig, H. Helm, and D. L. Huestis, Rev. Sci. Instrum. **67**, 2257 (1996).
[25] J. Winterhalter, D. Maier, J. Honerkamp, V. Schyja, and H. Helm, J. Chem. Phys. **110**, 11 187 (1999).
[26] M. J. J. Vrakking, Rev. Sci. Instrum. **72**, 4084 (2001).
[27] M. J. J. Vrakking, J. Phys. Chem. **101**, 6761 (1997).
[28] C. Jugen, *Molecular Applications of Quantum Defect Theory* (IOP, Bristol, 1996).
[29] Y. Aharonov and D. Bohm, Phys. Rev. **115**, 485 (1959).
[30] G. M. Lankhuijzen and L. D. Noordam, Phys. Rev. Lett. **76**, 1784 (1996).